Applied Catalysis B: Environmental 227 (2018) 409–417

Contents lists available at ScienceDirect

Applied Catalysis B: Environmental

journal homepage: www.elsevier.com/locate/apcatb

Highly loaded PbS/Mn-doped CdS quantum dots for dual application in solar-to-electrical and solar-to-chemical energy conversion

Jae-Yup Kim[a,1], Youn Jeong Jang[b,1], Jongwoo Park[c], Jeehye Kim[b], Jin Soo Kang[d,e], Dong Young Chung[d,e], Yung-Eun Sung[d,e], Changhee Lee[f], Jae Sung Lee[b,*], Min Jae Ko[g,*]

[a] Division of Chemical Engineering, Hoseo University, Asan-si, Chungcheongnam-do, 31499, Republic of Korea
[b] Department of Energy and Chemical Engineering, Ulsan National Institute of Science and Technology (UNIST), 50 UNIST-gil, Ulsan, 44919, Republic of Korea
[c] School of Chemical & Biomolecular Engineering, Georgia Institute of Technology, Atlanta, GA, 30332, USA
[d] Center for Nanoparticle Research, Institute for Basic Science (IBS), Seoul, 08826, Republic of Korea
[e] School of Chemical and Biological Engineering, Seoul National University, Seoul, 08826, Republic of Korea
[f] Department of Electrical and Computer Engineering, Seoul National University, 1 Gwanak-ro, Gwanak-gu, Seoul, 08826, Republic of Korea
[g] Department of Chemical Engineering, Hanyang University, 222 Wangsimri-ro, Seongdong-gu, Seoul, 04763, Republic of Korea

ARTICLE INFO

Keywords:
Quantum dots
Photoelectrochemical water splitting
Solar cells
Quantum dot loading

ABSTRACT

Among the various renewable sources of energy, solar energy conversion systems have been regarded as a promising way to satisfy the growing energy demand. For superior solar energy conversion performance, it is important to utilize efficient photosensitizers that have excellent light-harvesting capability. In this regard, quantum dots (QDs) are promising photosensitizer candidates owing to their high absorption coefficient, band gap tunability, and potential multiple exciton generation. Here, we report an effective and straightforward approach to improve the loadings of nanocomposite PbS/CdS QDs in a mesoporous electrode, for highly efficient solar energy conversion. By controlling the surface charge of TiO_2 during the successive ionic layer adsorption and reaction process, both the PbS and CdS QD loadings are distinctly increased, leading to a highly enhanced light-harvesting capability of the photoelectrodes. This enhancement is effectively applied not only for solar-to-electrical but also for solar-to-chemical energy conversion, resulting in a ~33% increased conversion efficiency of the QD solar cells and an unprecedented photocurrent of 22.1 mA/cm^2 (at 0.6 V vs. RHE) for hydrogen production from photoelectrochemical water splitting. These results provide significant insight into the application of QD photosensitizers in solar energy conversion.

1. Introduction

Currently, the increasing global energy demand and the environmental degradation caused by the use of fossil fuels have led to an urgent need for the development of clean and abundant renewable sources of energy. Among the various such sources, solar energy conversion has been regarded as a promising way to satisfy the growing energy demand owing to the renewable, inexpensive, and nonpolluting properties of sunlight. The most common method for solar energy conversion is the utilization of photovoltaics to directly convert the solar light into electricity [1–20]. In particular, the development of low-cost and high efficiency photovoltaics, such as dye-sensitized solar cells [1–5], quantum dot solar cells [6–11], organic solar cells [12,13], and perovskite solar cells [14–20] have been intensively studied.

Another important use of solar energy is hydrogen production via photoelectrochemical (PEC) water splitting, which can be categorized as solar-to-chemical conversion [21–38]. In general, the water electrolysis reaction is composed of two half reactions, the oxygen evolution reaction and the hydrogen evolution reaction. Since the first report on the use of the single-crystal TiO_2 as a catalyst for PEC water splitting in 1972 [21], various semiconductor materials, including TiO_2 [22,23], Fe_2O_3 [24–26], ZnO [27–29], WO_3 [30–32], and $BiVO_4$ [33–37], have been studied for the development of efficient photoelectrodes.

To achieve high efficiencies for both solar-to-electrical and solar-to-chemical energy conversions, it is firstly important to utilize efficient photosensitizers to ensure the superior light-harvesting capability of the photoelectrodes. In this regard, quantum dots (QDs) are attractive photosensitizer candidates owing to their unique optoelectronic properties, which include a high absorption coefficient, band gap tunability, and potential multiple exciton generation [6–11,39–41]. Furthermore,

* Corresponding authors.
E-mail addresses: jlee1234@unist.ac.kr (J.S. Lee), mjko@hanyang.ac.kr (M.J. Ko).
[1] These authors contributed equally to this work.

https://doi.org/10.1016/j.apcatb.2018.01.041
Received 13 November 2017; Received in revised form 4 January 2018; Accepted 18 January 2018
Available online 31 January 2018
0926-3373/

low-band-gap (< 1.5 eV) QDs, such as PbS [7,9,42], PbSe [41], and Cu-In-Se [10,11,43,44] QDs, can absorb over a wide spectral range, including the near-infrared region. One effective approach to solar energy conversion is the coating of QDs on the surface of mesoporous metal oxides, such as TiO_2, ZnO, and SnO_2, leading to a suitable architecture for efficient electron-hole pair separation and carrier transport [6,9–11,29,42–51]. Such QD-sensitized photoelectrodes have been intensively studied not only for QD-sensitized solar cells (QDSCs) but also for PEC water splitting.

The techniques used for the sensitization of mesoporous metal oxide films with QDs can be divided into two types: 1) direct growth of QDs onto the surface of metal oxide films via chemical bath deposition or successive ionic layer adsorption and reaction (SILAR) processes [42,45–48], and 2) deposition of presynthesized colloidal QDs via direct adsorption or with a bifunctional molecular linker [6,9–11,43,44]. These techniques have been applied to develop photoelectrodes decorated with various QDs, including CdSe [6], CdS [45,51], PbS [42,46], $CuInS_2$ [52], and Cu-In-Se [10,11,43,44], for application in QDSCs or PEC water splitting. In addition, various core-shell-structured or nanocomposite QDs, such as CdS/CdSe [47,53], CdTe/CdSe [9], $CuInS_2$/CdS [50], and PbS/CdS [48,54–56] have been studied with the aim of achieving synergy effects between the different compositions.

Although various compositions of QDs have been investigated and applied, the light-harvesting efficiency of photoelectrodes is fundamentally dependent on the QD loading on the surface of the mesoporous metal oxide films. To obtain a high photocurrent and efficiency for the solar energy conversion, it is firstly required to enhance the light-harvesting efficiency of the photoelectrode by depositing the QDs as densely as possible onto the photoelectrode. Here we describe an effective and straightforward approach to improve the loadings of nanocomposite PbS/CdS QDs on a mesoporous electrode, for highly efficient solar energy conversion. The conventional SILAR process for the PbS/CdS coating is modified by introduction of Mn-doping source and a pretreatment of mesoporous electrode with a basic solution. These modifications control the surface charge of mesoporous TiO_2 electrode, resulting in increased QD loadings by ~14–47%. We also demonstrate the superiority and versatility of our approach by achieving a significant improvement of photoelectrochemical performance, when applied in both solar-to-electrical and solar-to-chemical conversion. As a result of the increased QD loadings, the conversion efficiency of QDSCs is enhanced by approximately 33%. Furthermore, when applied in PEC water splitting as a photoanode, a remarkable photocurrent density of 22.1 mA/cm^2 (at 0.6 V vs. RHE) is obtained for hydrogen production, which is the highest value ever reported in QD studies.

2. Methods

2.1. Preparation of mesoporous TiO_2 electrodes

Three types of TiO_2 pastes were prepared for the fabrication of the mesoporous TiO_2 electrodes. First, a transparent paste containing TiO_2 particles of 20 nm diameter was prepared according to the procedure described in a previous paper [57]. In brief, nanocrystalline TiO_2 particles were synthesized by a hydrothermal process, followed by mixing with ethyl cellulose (Aldrich), lauric acid (Fluka) and α-terpineol (Fluka). The weight ratio of the compositions was as follows: TiO_2/ethyl cellulose/lauric acid/α-terpineol = 0.18/0.05/0.02/0.75. Furthermore, a scattering paste was prepared with TiO_2 particles of 500 nm diameter (G2, Showa Denko, Japan). In addition, a mixed paste was prepared by mixing TiO_2 particles of 20 and 500 nm diameters in the ratio 1:1 (w/w). All other constituents of the scattering and mixed pastes were identical to those of the transparent paste. Before the deposition of these pastes, a fluorine-doped tin oxide (FTO) glass (Pilkington, TEC-8, 8 Ω/sq) was pretreated by spin coating with 7.5 wt% Ti (IV) bis(ethyl acetoacetato)-diisopropoxide solution in 1-butanol to form a dense blocking layer. The transparent paste was firstly deposited onto this substrate by the doctor blade technique, followed by the deposition of the mixed and scattering pastes in sequence. Then, the deposited TiO_2 pastes were annealed at 500 °C for 30 min in air. The thickness of the annealed TiO_2 film was measured using an Alpha-Step IQ surface profiler (KLA Tencor). In addition, to obtain a high performance of PEC water splitting, the annealed TiO_2 film was dipped into a 0.04 M TiC_4 aqueous solution at 70 °C for 30 min, followed by an additional annealing at 500 °C for 1 h. Furthermore, the substrate was modified from FTO glass into Ti metal foil (Goodfellow, 99.6% purity, 0.25 mm thick, and 2.5 cm × 2.5 cm in size).

2.2. Deposition of PbS/Mn-doped CdS QDs

The PbS/CdS QDs were deposited onto the surface of the mesoporous TiO_2 electrode by the SILAR technique, as described in previous reports [54]. For the PbS deposition, the TiO_2 electrode was dipped into a 0.02 M $Pb(NO_3)_2$ (Aldrich) methanol solution for 1 min and thoroughly washed with methanol. Subsequently, the electrode was dipped into a solution of 0.02 M Na_2S (Aldrich) in methanol/deionized (DI) water (1:1, v/v) for 1 min and washed with methanol. This cycle was repeated three times. To increase the PbS QD loading, one additional step was introduced into this typical PbS SILAR process: before every immersion in the $Pb(NO_3)_2$ solution, the TiO_2 electrode was pretreated by dipping in NaOH methanol solution (20–80 mM) for 1 min. For the CdS deposition, the PbS-sensitized electrode was dipped into a 0.5 M Cd $(NO_3)_2{\cdot}4H_2O$ (Aldrich) ethanol solution for 5 min and thoroughly washed with ethanol. Subsequently, the electrode was immersed into a 0.5 M Na_2S aqueous solution for 5 min and washed with DI water. This cycle was repeated three times. For the deposition of the Mn-doped CdS QDs, $(CH_3COO)_2Mn{\cdot}4H_2O$ (Aldrich) was added into the 0.5 M Cd $(NO_3)_2{\cdot}4H_2O$ (Aldrich) ethanol solution, resulting in 95 and 190 mM manganese ions. Finally, the QD-sensitized electrode was passivated with ZnS by dipping in a 0.1 M $Zn(CH_3COO)_2{\cdot}2H_2O$ (Aldrich) aqueous solution for 1 min and washed with DI water. Next, the electrode was immersed into a 0.1 M Na_2S aqueous solution for 1 min and washed with DI water. This cycle was repeated twice.

2.3. Fabrication of QDSCs

The Cu_2S counter-electrode was prepared by etching brass foil (Alfa Aesar, 0.25 mm thick) in a HCl solution (DAEJUNG, 35–37 wt%) at 70 °C for 25 min. The etched foil was washed with DI water and dried with a nitrogen flow. An aqueous polysulfide solution of 1M Na_2S and 1M S (99.998%, Aldrich) was dropped onto this foil, forming a porous Cu_2S film on its surface. The QD-sensitized TiO_2 electrode was assembled with the Cu_2S counter-electrode using hot-melt Surlyn (Dupont 1702, thickness ~60 μm). Then, an aqueous polysulfide electrolyte of 1 M Na_2S and 1 M S was injected into the assembled cells through two small holes that had been pre-drilled on the working electrode. The active area of each cell was in the range of 0.30 ± 0.03 cm^2, which was measured by using an image analysis program equipped with a CCD camera (Moticam 1000).

2.4. Characterization

The morphology of the deposited QDs on the TiO_2 nanoparticles and their surface compositions were examined by a high-resolution transmission electron microscopy (HR-TEM; JEOL JEM-2010) system equipped with energy-dispersive spectroscopy (EDS). The surface compositions on the vertical side of the TiO_2 electrode were examined with EPMA (JEOL JXA-8500F). The absorption property of the QD-sensitized TiO_2 electrode was analyzed by UV–vis spectroscopy (Agilent 8453). The QD loadings and surface electronic states were investigated and compared with XPS (PHI 5000 VersaProbe). The elemental composition of the QDs was examined with inductively coupled plasma optical emission spectrometry (ICP-OES; Thermo Scientific iCAP-7000).

X-ray absorption near-edge structure (XANES) analyses were performed by synchrotron measurements in the 10C beamline of the Pohang Accelerator Laboratory.

2.5. Evaluation of QDSC performance

Photocurrent density–voltage (*J–V*) measurements were performed using a solar simulator (Yamashita Denso YSS-200A) with a 1600 W Xenon lamp equipped with an AM 1.5G filter at 1 sun light intensity (100 mW/cm^2). Before this measurement, a black tape mask with an aperture was attached onto the front side of each cell to avoid overestimation caused by the additional illumination through the lateral space [58,59]. The incident photon-to-current conversion efficiency (IPCE) was measured under short-circuit conditions as a function of wavelength from 300 to 1200 nm using a specially designed system with a 75 W Xenon lamp source and a grating monochromator (PV Measurements Inc.).

2.6. Evaluation of PEC water splitting performance

The QD-sensitized TiO_2 electrodes were used for solar hydrogen evolution in the three-electrode configuration with a saturated calomel reference electrode (SCE) and a Pt mesh as the counter-electrode. The Ar-purged 0.25 M Na_2S and a 0.35 M Na_2SO_3 aqueous solution (pH ~12.5) was used as the standard electrolyte, while 0.5 M Na_2SO_4 aqueous solution (pH ~6.0) was used as a nonsacrificial electrolyte. The PEC hydrogen production was tested under the simulated 1 sun illumination using an AM 1.5G filtered solar simulator (91–160, Oriel). For the application of external bias to the system, a potentiostat (IviumStat, Ivium Technologies) was used. The evolved hydrogen was detected by gas chromatography (HP 7890) with a TCD (molecular sieves with a 5 Å column, Ar carrier gas) during the chronoamperometry test.

3. Results and discussion

Fig. 1 compares the HR-TEM images of the bare and QD (PbS/CdS) sensitized TiO_2 nanoparticles after ZnS treatment. A mesoporous electrode with 20-nm-diameter TiO_2 particles was coated with the QDs using the conventional SILAR process and was then peeled off from the substrate for the TEM analysis. We confirmed that the QDs, which had sizes of 5–6 nm, were homogeneously deposited on the surface of the TiO_2 nanoparticles. In addition, the surface compositions – that is, the presence of Pb, Cd, Zn, and S – were confirmed by the EDS analysis.

We firstly optimized the structure of the TiO_2 electrode for high photovoltaic performance by using three types of TiO_2 paste: transparent (20-nm-sized TiO_2), scattering (500-nm-sized TiO_2), and mixed paste (mixture of 20- and 500-nm-sized TiO_2). These pastes were deposited on the FTO glass in sequence with the doctor blade technique and the thickness of each layer was controlled using a frame of Scotch 3 M tape. The *J–V* characteristics of the PbS/CdS QDSCs depending on the structure of the TiO_2 electrode are shown in Fig. S1a and the results are summarized in Table S1. As listed in Table S1, the short-circuit current (J_{SC}) was enhanced as the thickness of the transparent layer was increased owing to the increase of the number of QD adsorption sites. However, the open-circuit voltage (V_{OC}) was reduced as the thickness of the transparent layer was increased, which was attributed to the increase of the number of electron recombination sites [60,61]. As shown in Fig. S1a, the dark current gradually increased with increasing TiO_2 film thickness, indicating that the electron recombination rate became gradually faster [62]. As a result, the conversion efficiency (η) was optimized to 4.00% for the electrode structure of sample PbS/CdS-2, depicted in Fig. S1b. Although sample PbS/CdS-4 had a similar total TiO_2 film thickness with PbS/CdS-2, it exhibited lower J_{SC} and conversion efficiency, indicating that the presence of the mixed layer between the transparent and scattering layers is advantageous for the efficient utilization of the incident light. These results determined the electrode structure PbS/CdS-2 as the optimum one; therefore, further investigations were performed on this optimum structure. In addition, the IPCE spectra of PbS/CdS-2 and CdS-only (Fig. S1c) and their comparison with the literature [55,63,64] enabled us to determine an approximate energy level alignment for the PbS/CdS-sensitized TiO_2 electrode, as shown in Fig. S1d.

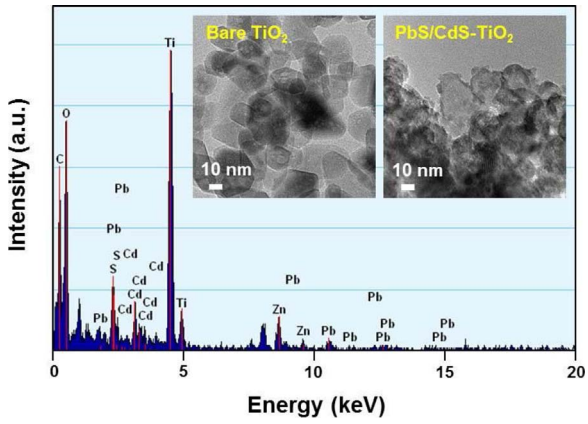

Fig. 1. Quantitative surface composition of PbS/CdS-sensitized TiO_2 nanoparticles after ZnS treatment, measured with EDS. Inset: HR-TEM images of bare TiO_2 and PbS/CdS-sensitized TiO_2 nanoparticles.

To enhance the photoconversion properties of the CdS layer, we introduced Mn as a dopant by adding the Mn precursor into the Cd^{2+} precursor solution used for the SILAR process. As shown in Fig. S2, the absorbance of CdS increased by the Mn doping. Fig. 2a shows the *J–V* characteristics of the PbS/Mn-doped CdS QDSCs as a function of the Mn content and the results are summarized in Table 1. The nominal molar ratio between Cd and Mn – that is, the ratio between Cd^{2+} and Mn^{2+} ions dissolved in the cationic precursor solution for the Mn-doped CdS SILAR process – was 1:0.38 (PbS/Mn-CdS-1) and 1:0.75 (PbS/Mn-CdS-2). Further addition of Mn into the cationic precursor solution was impossible owing to the solubility limitation of ethanol. As displayed in Table 1, V_{OC} was almost unchanged but J_{SC} was greatly enhanced as the content of Mn was increased, resulting in a gradual increase of the conversion efficiency. Compared to the reference (PbS/CdS), J_{SC} and the conversion efficiency were enhanced by approximately 23 and 10%, respectively, for PbS/Mn-CdS-2. Fig. 2b compares the IPCE spectra of the undoped (PbS/CdS) and Mn-doped (PbS/Mn-CdS-2) samples. Both samples exhibited a broad absorption spectrum up to a wavelength of approximately 1200 nm, which was attributed to the narrow band gap of PbS. The Mn-doped sample showed enhanced IPCE compared to the undoped one in the wavelength range 400–850 nm, suggesting that the photocurrent generated from CdS was increased by the Mn doping.

The Mn doping method has been applied in previous studies for the preparation of efficient Mn-doped CdS [65,66], Mn-doped CdS/CdSe [53], and $CuInS_2$/Mn-doped CdS [67] QDSCs. In these studies, the Mn-doped CdS layer was deposited with the SILAR method and the Mn doping resulted in the enhancement of light absorption and J_{sc}, which is consistent with our results. However, all previous studies attributed the enhanced photovoltaic properties produced by Mn doping to the improved electronic property of the QDs. The authors reported that Mn doping creates midgap states in CdS and the transition between the energy levels of this midgap ($^4T_1$–$^6A_1$) is both spin- and orbital-forbidden, resulting in reduced charge recombination with the electrolyte. On the other hand, in this study, we investigated the influence of Mn doping from the perspective of QD loading. Fig. 3 shows the cross-sectional EPMA images of the PbS/Mn-doped CdS QD-sensitized TiO_2 electrode depending on the Mn content. The figure clearly shows that the QD loading increased in the order scattering layer < mixed layer < transparent layer owing to the differences between the surface

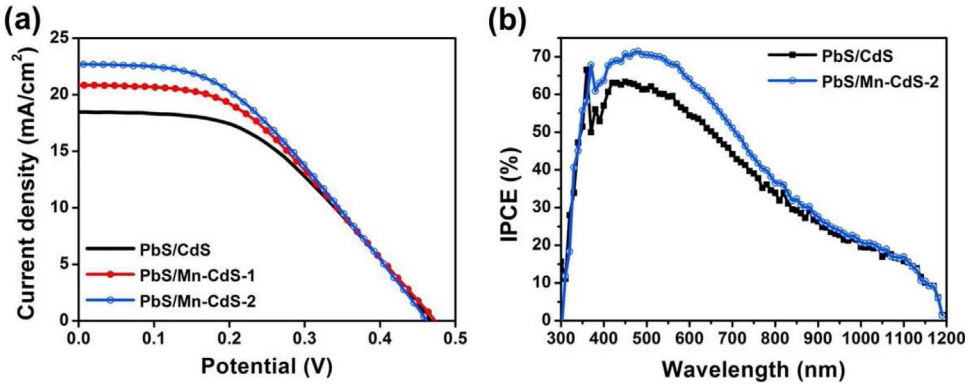

Fig. 2. (a) *J–V* characteristics under illumination (light intensity 100 mW/cm^2, AM 1.5 G filter) and (b) IPCE spectra of PbS/Mn-doped CdS QDSCs depending on Mn content, as detailed in Table 1.

Table 1
Summary of *J–V* characteristics for PbS/Mn-doped CdS QDSCs depending on the Mn content.

Sample	Nominal molar ratio of Cd:Mn	J_{SC} (mA/cm^2)	V_{OC} (V)	*FF* (%)	η (%)
PbS/CdS	–	18.48	0.47	46	4.00
PbS/Mn-CdS-1	1:0.38	20.84	0.47	43	4.21
PbS/Mn-CdS-2	1:0.75	22.71	0.46	42	4.39

areas of each layer. Interestingly, the detected S and Cd were greatly increased by the Mn doping, indicating that the CdS QD loading was largely enhanced. Compared to PbS/Mn-CdS-1, PbS/Mn-Cd-2 exhibited slightly lower Cd content and higher Mn content, suggesting that the adsorption of Cd^{2+} ions was slightly reduced owing to the increase in Mn^{2+} ions during the SILAR process.

To quantitatively compare the CdS QD loading with respect to the Mn content, we performed XPS analysis. Fig. 4a shows the spectra of the PbS/Mn-doped CdS QD-sensitized TiO_2 electrodes over a wide scan range. All spectra exhibit the presence of Ti, O, Pb, Cd, S, and C. However, no peaks corresponding to Mn were observed in the Mn-doped samples, which can be attributed to the small amount of Mn species or to overlapping with the Cd peaks. Fig. 4b and c show the high-resolution Pb 4f and Cd 3d spectra, respectively. The binding energy (BE) values for each sample are listed in Table 2. The BEs of Pb $4f_{7/2}$ were in the range 138.0–138.1 eV, which corresponds to Pb—S bonds [68]. In addition, the BEs of Cd $3d_{5/2}$ were in the range 404.5–404.7, which corresponds to Cd-S bonds [69]. In Fig. 4d, it is noticeable that the Cd 3d peaks shift toward lower BEs because of the Mn doping. Since the electronegativity of Mn ($\chi_P = 1.55$) is lower than that of S

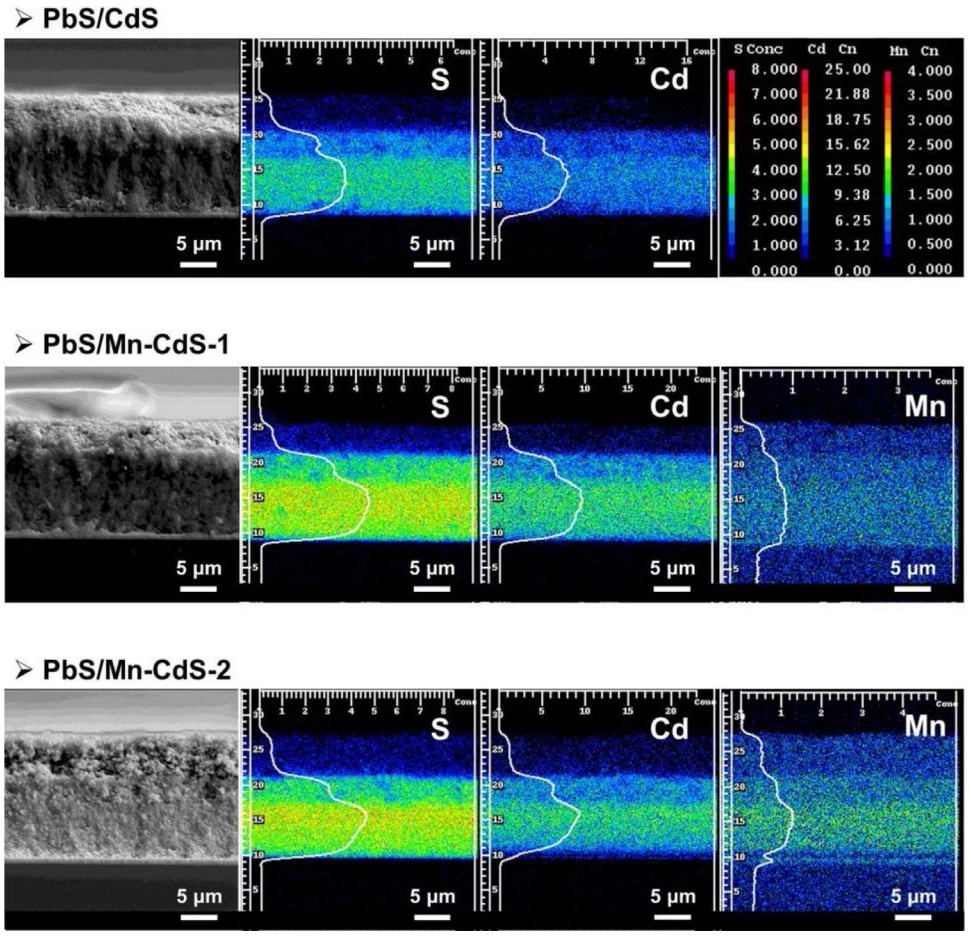

Fig. 3. Sulfur, cadmium, and manganese EPMA images of PbS/Mn-doped CdS QD-sensitized TiO_2 electrodes depending on Mn content. The graphs display the atomic concentrations of the corresponding elements.

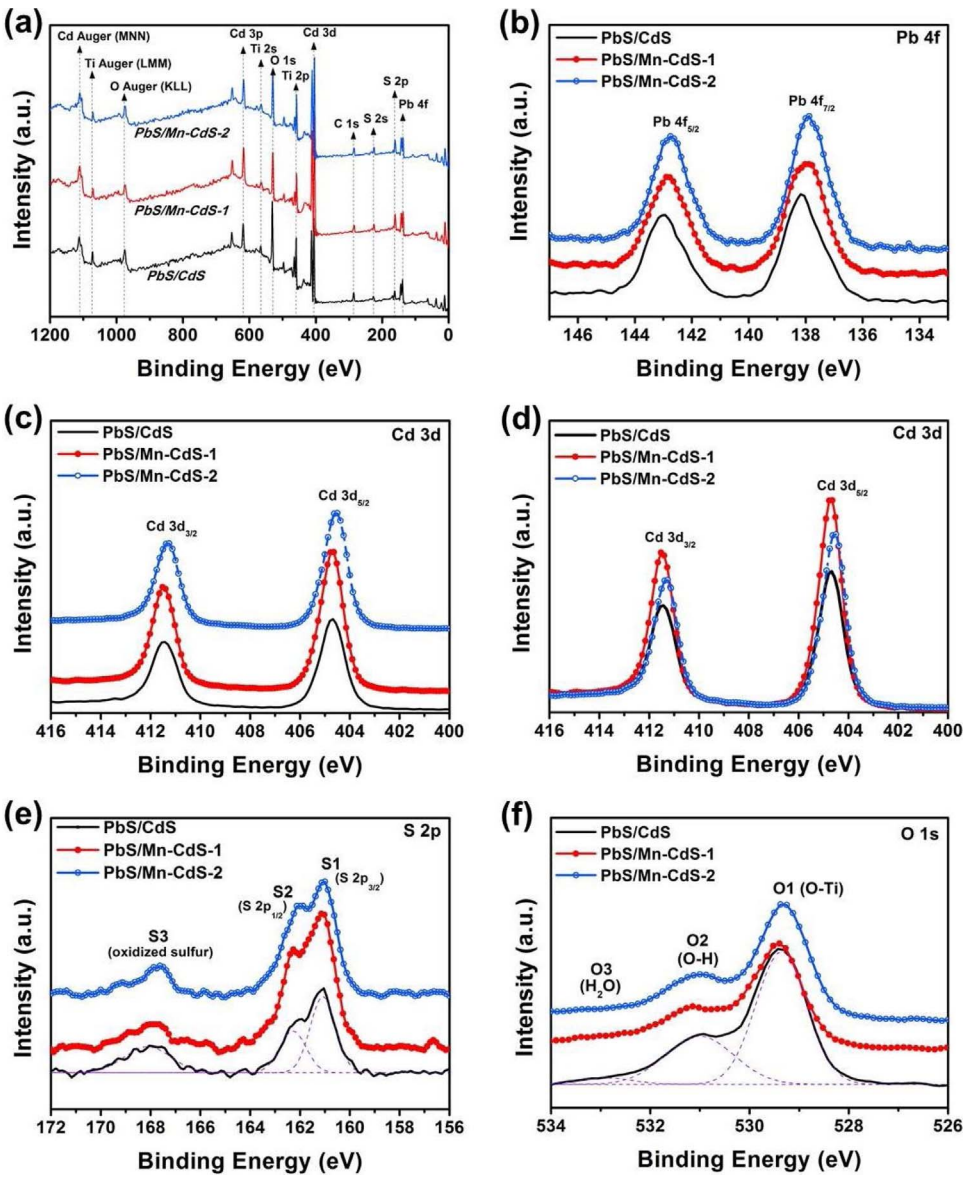

Fig. 4. XPS spectra of PbS/Mn-doped CdS QD-sensitized TiO_2 electrodes depending on Mn content. (a) Survey scan. High-resolution scans of (b) Pb 4f and (c) Cd 3d region. (d) Revised plot of (c) after matching the baseline. High-resolution scans of (e) S 2p and (f) O 1s.

(χ_P = 2.56), the Cd atoms bonded to Mn are expected to appear at a lower energy than the Cd atoms bonded to S, resulting in the observed peak shift toward lower Bes [70]. Furthermore, the Cd 3d peak area clearly increases with Mn doping in the order PbS/CdS < PbS/Mn-CdS–2 < PbS/Mn-CdS-1, which is consistent with the EPMA data. Quantitative analysis on the Cd $3d_{5/2}$ peak area revealed that the content of Cd atoms increased by 44% and 25% for PbS/Mn-CdS-1 and PbS/Mn-CdS-2, respectively, compared to the undoped sample (PbS/CdS), meaning that the CdS QD loading were considerably enhanced by the introduction of Mn-doping source. Therefore, it is reasonable to consider that the enhanced absorbance and photocurrent achieved by the incorporation of Mn resulted not only from the doping effect of Mn (creation of midgap states) but also from the increase in CdS QD loading.

Fig. 4e shows the high-resolution S 2p spectra, which can be deconvoluted into three different peaks, as shown in Fig. S3a–c. The BEs of S $2p_{3/2}$ were in the range 161.1–161.2 eV, which corresponds to S—Pb or S—Cd bonds [71,72]. The S 2p peaks at 167.9–168.1 eV correspond to oxidized sulfur groups [73], indicating that the surface of the CdS QDs was partially oxidized. Fig. 4f shows the high resolution O 1s spectra, which can be deconvoluted into three different peaks, as shown in Fig. S3d–f. The BEs of these peaks were almost equal for all samples, as listed in Table 2. The peaks at 529.3–529.4, 531.0, and 532.9 eV correspond to the O—Ti bond [74], hydroxyl group (OH^-) [75], and chemisorbed water [76], respectively.

Since XPS is a technique chiefly for surface analysis, a more exact

Table 2
BE values obtained from the XPS analysis for the PbS/Mn-doped CdS QD-sensitized TiO_2 films depending on the Mn content.

Sample	Pb $4f_{7/2}$	Cd $3d_{5/2}$	S $2p_{3/2}$	S3 (S-O)	O 1s (O-Ti)	O 1s (O-H)	O 1s (H_2O)
PbS/CdS	138.1 eV	404.7 eV	161.1 eV	168.1 eV	529.4 eV	531.0 eV	532.9 eV
PbS/Mn-CdS-1	138.0 eV	404.7 eV	161.2 eV	168.0 eV	529.4 eV	531.0 eV	532.9 eV
PbS/Mn-CdS-2	138.0 eV	404.5 eV	161.1 eV	167.9 eV	529.3 eV	531.0 eV	532.9 eV

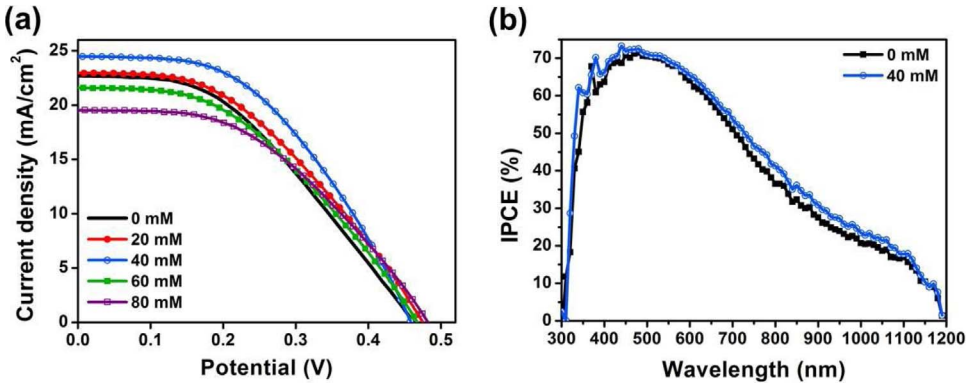

Fig. 5. (a) *J–V* characteristics under illumination (light intensity 100 mW/cm^2, AM 1.5 G filter) and (b) IPCE spectra of PbS/Mn-doped CdS QDSCs depending on the concentration of the NaOH solution used for pretreatment in the SILAR process.

estimation of increased CdS QD loading was determined from ICP-OES results, as listed in Table S2. The relative CdS QD loading on the mesoporous TiO_2 film was represented by Cd/Ti atomic ratio. The Cd/Ti atomic ratio was increased by 35% and 14% for PbS/Mn-CdS-1 and PbS/Mn-CdS-2, respectively, compared to the undoped sample (PbS/CdS). This indicates that the CdS QD loading was enhanced by 35% and 14%, respectively. The Mn/Ti atomic ratio of PbS/Mn-CdS-2 was about 2 times greater than that of the PbS/Mn-CdS-1, meaning that the coadsorbed Mn content was nearly doubled. This increase is in good agreement with the relative amounts of Mn content in the cationic precursor solutions. As a result, the atomic ratio between total cations (Cd + Mn) and Ti was enhanced by 45% and 35% for PbS/Mn-CdS-1 and PbS/Mn-CdS-2, respectively, compared to PbS/CdS.

The doping effect of Mn was validated by the XANES spectra. Fig. S4 shows the Cd K-edge in the XANES spectra and their first derivatives for CdS (undoped) and Mn-doped CdS QD-sensitized TiO_2 electrodes. The edge energy is defined as the energy positions of the peak maximum in the first derivative curves [77]. As shown in Fig. S4c, the edge energy of Mn-CdS-1 is almost the same as that of the undoped CdS sample. On the other hand, the edge energy of Mn-CdS-2 is slightly shifted toward a lower photon energy, indicating a decrease in the valence number of the Cd species due to the Mn ion doping. This trend is in accordance with the XPS analysis results, as discussed above. Both the peak positions in the Cd 3d region of the XPS spectrum and the edge energy of the Cd K-edge XANES spectrum are almost the same for the undoped CdS sample and Mn-CdS-1. In the case of Mn-CdS-2, both peaks are slightly shifted compared to that of the undoped CdS sample. These results indicate that the doping level of Mn in the CdS lattice was low for the Mn-doped CdS QDs, especially for Mn-CdS-1. Thus, it can be concluded that the enhanced photovoltaic properties of the Mn-doped CdS QDs can be attributed to both the doping effect of Mn and the increase in CdS QD loading; however, the contribution of the latter was relatively greater.

Then, why does the addition of the Mn source during the SILAR process enhance the QD loading? To determine the origin of this behavior, we investigated the influence of the Mn source on the pH of the Cd^{2+} precursor solution. We measured the pH of the Cd^{2+} precursor solution (0.5M $Cd(NO_3)_2{\cdot}4H_2O$ ethanol solution) with respect to the concentration of the added Mn source ($(CH_3COO)_2Mn{\cdot}4H_2O$), as shown in Fig. S5. The pH value of the precursor solution was greatly increased by the addition of the Mn source. The pH of the precursor solutions used for the fabrication of CdS, Mn-CdS-1, and Mn-CdS-2 was 2.54, 4.43, and 4.56, respectively. All of these pH values are lower than the point of zero charge (pzc) of TiO_2 (~6) [78]; therefore, the surface of the TiO_2 electrode was positively charged in these precursor solutions. The positive surface charge is unfavorable for the efficient adsorption of cations (Cd^{2+}) and resulting QD loading owing to the repulsive electrostatic force [79]. However, the surface of the TiO_2 electrode becomes less positively charged in a precursor solution with a relatively higher pH value, resulting in the decrease of the repulsive electrostatic force acting on the cationic ions. Therefore, a relatively larger amount of Cd^{2+} ions can be adsorbed on the surface of the TiO_2 electrode in the precursor solutions used for Mn-CdS-1 and Mn-CdS-2 compared to that used for pure CdS, leading to the enhanced CdS QD loading.

Although the photocurrent and conversion efficiency were enhanced by the addition of Mn species, the light harvesting in the long-wavelength region above 850 nm was not improved, as confirmed by the IPCE spectra (Fig. 2b). This is attributed to the relatively large band gap of CdS. To achieve further photovoltaic performance enhancement by increasing the light harvesting in the long-wavelength region, it is necessary to increase the loading of the PbS QDs that have a relatively low band gap. For this purpose, we used a basic solution to negatively charge the surface of TiO_2 during the Pb^{2+} coating process. First, we added TEA into the cationic (Pb^{2+}) precursor solution used for the SILAR process to enhance the PbS QD loading, according to the method described in a previous paper [79]. However, we determined that this method is not applicable to relatively thick TiO_2 films (thickness > 10 μm) because the viscosity of the cationic precursor solution was greatly increased by the addition of TEA. Instead, we considered adding NaOH or KOH, which do not affect the viscosity of the Pb^{2+} precursor solution. However, this approach was also not applicable because the Pb^{2+} precursor was precipitated in the presence of NaOH or KOH.

Finally, we introduced a modified SILAR process for the deposition of the PbS QDs, in which the mesoporous TiO_2 film was dipped into a NaOH methanol solution for 1 min before every immersion in the Pb $(NO_3)_2$ solution. Fig. 5a shows the *J–V* characteristics of the PbS/Mn-doped CdS QDSCs with respect to the concentration of the NaOH solution used for pretreatment in the SILAR process and the results are summarized in Table 3 (the doping level of Mn was the same as in the case of Mn-CdS-2). By using this modified SILAR process, the V_{OC} of the DSSCs was not greatly affected; however, the J_{SC} and fill factor (*FF*) were improved. As a result, the pretreatment with the 40 mM NaOH solution improved J_{SC} and the conversion efficiency by ~8 and 21%, respectively, compared to the reference. This enhanced photovoltaic performance was attributed to the increased PbS QD loading, which was confirmed by visual inspection (Fig. S6), the EPMA images, and the XPS analysis (Fig. 6), as will be discussed later. As shown in Fig. 5b, the IPCE of the DSSC prepared with the modified SILAR process was slightly higher than that of the reference, particularly in the longer-

Table 3
Summary of *J–V* characteristics for PbS/Mn-doped CdS QDSCs depending on the concentration of the NaOH solution used for pretreatment in the SILAR process.

Concentration of NaOH solution (mM)	J_{SC} (mA/cm^2)	V_{OC} (V)	*FF* (%)	η (%)
reference	22.71	0.46	42	4.39
20	22.95	0.48	43	4.74
40	24.53	0.46	47	5.30
60	21.57	0.47	43	4.36
80	19.54	0.48	45	4.22

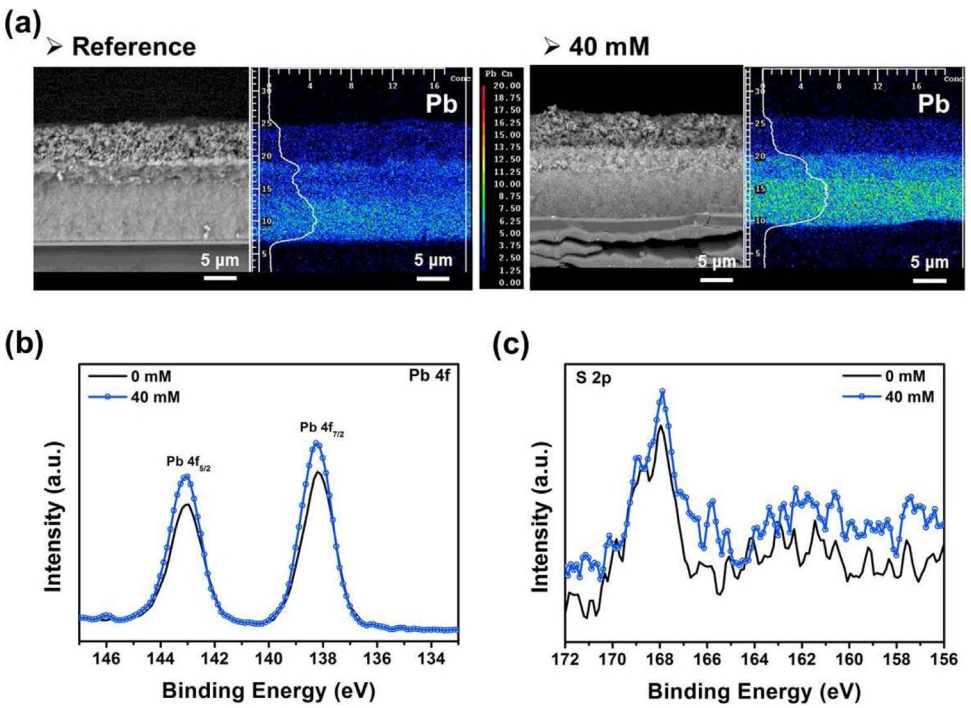

Fig. 6. (a) Lead EPMA images and high-resolution XPS spectra of (b) Pb 4f and (c) S 2p region for PbS QD-sensitized TiO_2 electrodes prepared with the conventional and modified (pretreated with 40 mM NaOH solution) SILAR processes.

wavelength region (650–1100 nm). This result confirms that the enhanced J_{SC} resulted from the increased PbS QD loading.

Fig. 6a compares the cross-sectional Pb EPMA images of a PbS QD-sensitized TiO_2 electrode prepared with the conventional and the modified (pretreated with 40 mM NaOH solution) SILAR processes. It is obvious that the adsorbed Pb species was increased by the modified process. In addition, the peak intensities in the XPS spectra of both the Pb 4f (Fig. 6b) and S 2p (Fig. 6c) regions increased for the electrode prepared with the modified process. The Pb 4f peak areas of these two electrodes had a ratio of 1:1.18, indicating the improved PbS QD loading by the modified SILAR process. In addition, the ICP-OES data revealed that the Pb/Ti atomic ratio in PbS QD-sensitized TiO_2 electrode was increased by 47% (Table S3). These results imply that the PbS QD loading was enhanced by approximately 47% with the modified SILAR process.

Finally, compared to the Pb/CdS QDSC prepared with the conventional process (J_{SC} = 18.48 mA/cm^2, η = 4.00%), both J_{SC} and the conversion efficiency were increased by approximately 33% (J_{SC} = 24.53 mA/cm^2, η = 5.30%) for the QDSC that was prepared with the modified process (Mn doping and pretreatment with NaOH solution), which was mainly attributed to the enhancement of the QD loading by ~35 and ~47% for CdS and PbS, respectively.

The improved light utilization resulting from the increased QD loading can be applied not only to photovoltaics but also to PEC hydrogen production. We applied the same strategy to a PEC hydrogen production system. The solar hydrogen production was tested in an Ar-pursed 0.25 M Na_2S and 0.35 M Na_2SO_3 aqueous solution, which was acting as the sacrificial reagent to prevent severe photocorrosion, under a simulated 1 sun illumination, as shown in Fig. 7. All measurements were performed under chopped irradiation to monitor the performance of the system in dark and light conditions simultaneously. To examine the influences of the Mn doping and the enhanced QD loading, three different types of QD-sensitized TiO_2 electrodes were compared; namely, with PbS/CdS QDs (labeled PbS/CdS), PbS/Mn-doped CdS QDs (enhanced CdS loading) (PbS/Mn-CdS), and PbS/Mn-doped CdS QDs prepared with the NaOH treatment (enhanced PbS and CdS loadings) (PbS(+)/Mn-CdS). In addition, the performance of the bare TiO_2 electrode was also measured.

The bare TiO_2 electrode showed a photocurrent of 1.98 mA/cm^2 at 1.23 V vs. RHE. The electrodes with CdS and PbS QDs exhibited dramatically enhanced solar-assisted performances, indicating the effective utilization of visible-light photons owing to their narrow band gaps relatively to that of TiO_2. However, as shown in Fig. 7a, an unexpected current was measured in dark conditions. To investigate the effect of the QDs under solar irradiation, chronoamperometry measurements were conducted at 0.6 V vs. RHE and no dark current was observed (Fig. 7b). The photocurrents of PbS/CdS and PbS/Mn-CdS were evaluated to be approximately 6 and 7 times greater (12.04 and 14.23 mA/cm^2) than that of the bare TiO_2, respectively. Furthermore, the photocurrent of PbS(+)/Mn-CdS was estimated to be at least 9 times higher (17.92 mA/cm^2) than that of the bare TiO_2. Photogenerated electron and hole pairs were easily separated at the type-I junction of PbS and CdS, resulting in improved photo-induced performance [55]. In addition, solar energy utilization became more effective by combining CdS with PbS, which have narrow band gaps. Above all, the obtained data indicate that the enhanced solar energy utilization that results from the increased QD loading can be effectively applied to PEC hydrogen production as well as to solar cells.

The poor connection between TiO_2 nanoparticles and at the interface between TiO_2 and the substrate allows photogenerated charge trapping and recombination before the charge separation and transfer. To improve the photocatalytic performance, necking treatment and ohmic junction formation were suggested. First, the annealed TiO_2 film was treated with $TiCl_4$ to enhance necking between TiO_2 nanoparticles. Additionally, the substrate was modified from FTO glass to Ti metal foil. The post-modification results are exhibited in Fig. 8. Interestingly, the current in the dark condition was eliminated with this modification. Furthermore, the electrode fabricated on the Ti metal with the $TiCl_4$ treatment showed an enhanced photocurrent, especially in the lower bias region. The role of $TiCl_4$ treatment is to reduce the charge transfer resistance between TiO_2 nanoparticles, leading to easy electron transfer and enhanced performances. Moreover, due to the lower work function of Ti metal (4.33 eV) relatively to that of *n*-type TiO_2 (4.7–5.8 eV), an ohmic junction is formed, facilitating charge separation. As a result, an unprecedentedly high photocurrent density of 22.1 mA/cm^2 (at 0.6 V vs. RHE) was obtained.

To determine the actual hydrogen production ability, a chronoamperometry test of the post-modified electrode was conducted at

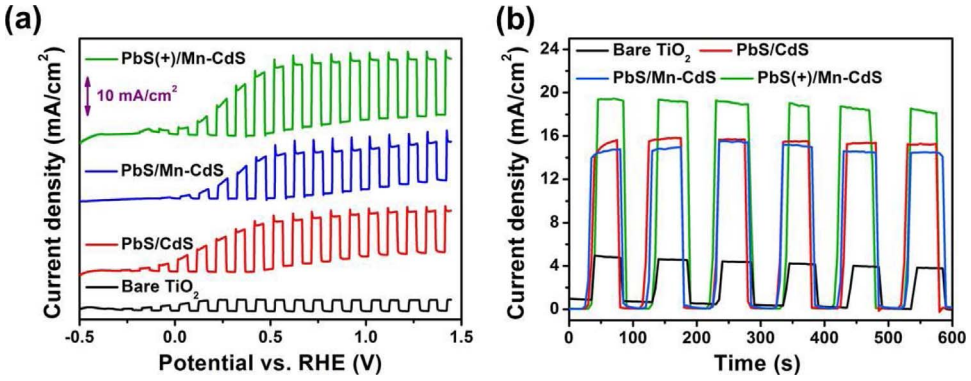

Fig. 7. (a) *J–V* characteristics and (b) chronoamperometric curves at 0.6 V vs. RHE of bare TiO_2, PbS/CdS, PbS/Mn-doped CdS (PbS/Mn-CdS), and PbS/Mn-doped CdS QDs prepared by the modified SILAR process (PbS(+)/Mn-CdS). The area of the electrode was ~0.25 cm^2.

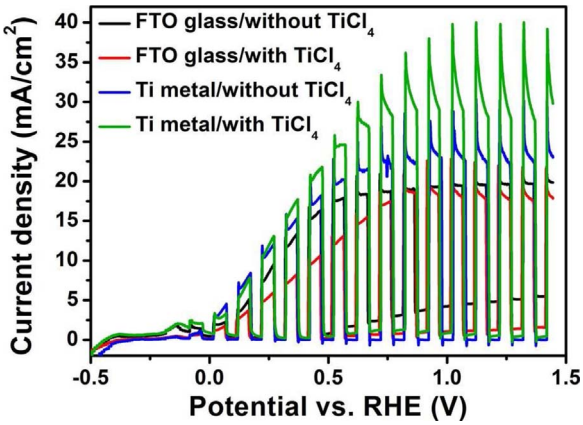

Fig. 8. *J–V* characteristics of PbS(+)/Mn-CdS electrodes for different types of substrates (FTO glass or Ti metal) and post-treatment ($TiCl_4$). The area of the electrode was ~0.25 cm^2.

0.4 V vs. RHE for 1 h (Fig. 9a) and the evolved hydrogen was detected during the reaction (Fig. 9b). Initially, the evolved gas was not fully collected owing to its low concentration, reflecting low faradaic efficiency (~84%). The faradaic efficiencies were almost preserved at 85–94%, which reveals that the major part of the photocurrent induced PEC hydrogen production. A degraded faradaic efficiency was expected because of insufficient gas collections caused by adsorption on the electrode or dissolution in the electrolyte, and self-corrosion of QDs. Despite this limitation, the QD-sensitized photoanode prepared in this work exhibited the highest ever reported photocurrent density for QD studies, as summarized in Table S4, which results from the superior light-harvesting capability of the highly loaded QD sensitizers.

In general, the solar hydrogen production of metal chalcogenide QDs is tested in an aqueous solution containing sacrificial reagents such as S^{2-} and SO_3^{2-}, since they suffer significant photocorrosion during the photocatalytic reaction [45–48,50,51,80]. Therefore, only a few studies examined the overall water splitting performance of metal chalcogenide QDs in a nonsacrificial electrolyte, as listed in Table S5. We also evaluated the overall water splitting performance of PbS/Mn-CdS QDs in a nonsacrificial electrolyte (0.5 M Na_2SO_4 aqueous solution). The *J–V* curves (Fig. S7a) show that the PbS(+)/Mn-CdS still exhibited higher photocurrent (2.0 mA/cm^2 at 0.6 V vs. RHE) than that of PbS/CdS (0.87 mA/cm^2). In addition, Fig. S7b and c show the amount of evolved hydrogen and oxygen gases at 0.4 V vs. RHE for PbS/CdS and PbS(+)/Mn-CdS, respectively. The H_2 to O_2 ratio was close to the expected 2:1 stoichiometry for both electrodes. Compared to the PbS/CdS, the PbS(+)/Mn-CdS exhibited the increased amounts of both hydrogen and oxygen gases. Furthermore, as summarized in Table S5, the obtained PEC water splitting performance without using sacrificial agents is excellent among QD photosensitizers.

4. Conclusions

In this study, we developed nanocomposite PbS/Mn-doped CdS QDs coated on TiO_2 electrodes with greatly improved QD loadings for application in solar energy conversion. The conventional SILAR process used for QD coating was modified to efficiently control the surface charge of mesoporous TiO_2 electrodes, leading to the increase in CdS and PbS QD loadings by approximately 35 and 47%, respectively; this improvement was confirmed by XPS and EPMA analyses. The superior light-harvesting capability arising from the improved QD loadings results in highly efficient photovoltaic and photocatalytic performances. When applied to QDSCs acting as a photoanode, the modified SILAR process leads to the increase of the conversion efficiency by ~33%. Furthermore, when applied in PEC water splitting, a remarkable photocurrent of 22.1 mA/cm^2 (at 0.6 V vs. RHE) is obtained for hydrogen production, which is the highest value ever reported in QD studies. We believe that the strategies proposed in this study can be applied not only to CdS and PbS QDs but can be generalized to various other types of QDs. In addition, these results demonstrate a substantial technological advancement and provide significant insight into the application of QD photosensitizers in solar energy conversion.

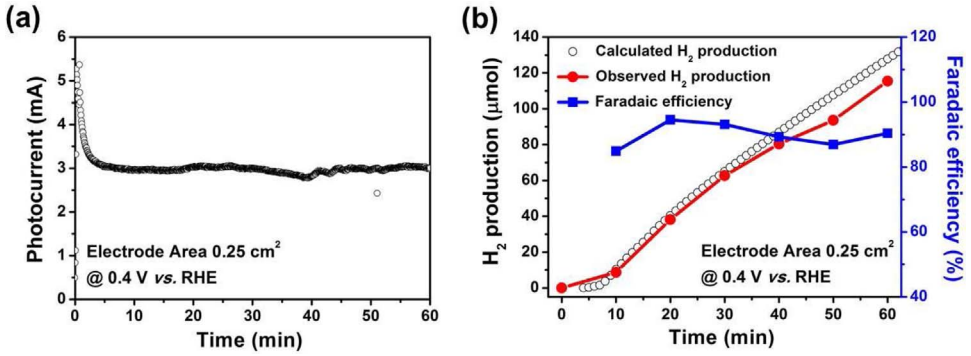

Fig. 9. (a) Chronoamperometry test result of actual hydrogen production measurement performed at 0.4 V vs. RHE for 1 h and (c) time-profiled hydrogen production and calculated faradaic efficiency of Pb(+)/Mn-CdS electrode, fabricated on a Ti metal substrate with $TiCl_4$ treatment. The area of the electrode was ~0.25 cm^2.

Acknowledgement

This work was also supported by the research fund of Hanyang University (HY-2017).

Appendix A. Supplementary data

Supplementary data associated with this article can be found, in the online version, at https://doi.org/10.1016/j.apcatb.2018.01.041.

References

[1] B. O'Regan, M. Grätzel, Nature 353 (1991) 737.
[2] A. Yella, H.-W. Lee, H.N. Tsao, C. Yi, A.K. Chandiran, M.K. Nazeeruddin, E.W.-G. Diau, C.-Y. Yeh, S.M. Zakeeruddin, M. Grätzel, Science 334 (2011) 629.
[3] Y. Li, D.-K. Lee, J.Y. Kim, B. Kim, N.-G. Park, K. Kim, J.-H. Shin, I.-S. Choi, M.J. Ko, Energy Environ. Sci. 5 (2012) 8950.
[4] K. Yoo, J.-Y. Kim, J.A. Lee, J.S. Kim, D.-K. Lee, K. Kim, J.Y. Kim, B. Kim, H. Kim, W.M. Kim, J.H. Kim, M.J. Ko, ACS Nano 9 (2015) 3760.
[5] J.-Y. Kim, J.Y. Lee, K.-Y. Shin, H. Jeong, H.J. Son, C.-H. Lee, J.H. Park, S.-S. Lee, J.G. Son, M.J. Ko, Appl. Catal. B: Environ. 192 (2016) 342.
[6] I. Robel, V. Subramanian, M. Kuno, P.V. Kamat, J. Am. Chem. Soc. 128 (2006) 2385.
[7] S.A. McDonald, G. Konstantatos, S. Zhang, P.W. Cyr, E.J.D. Klem, L. Levina, E.H. Sargent, Nat. Mater. 4 (2005) 138.
[8] C.M. Chuang, P.R. Brown, V. Bulovic, M.G. Bawendi, Nat. Mater. 13 (2014) 796.
[9] K. Zhao, Z. Pan, I. Mora-Seró, E. Cánovas, H. Wang, Y. Song, X. Gong, J. Wang, M. Bonn, J. Bisquert, X. Zhong, J. Am. Chem. Soc. 137 (2015) 5602.
[10] J.-Y. Kim, J. Yang, J.H. Yu, W. Haek, C.-H. Lee, H.J. Son, T. Hyeon, M.J. Ko, ACS Nano 9 (2015) 11286.
[11] J. Du, Z. Du, J.-S. Hu, Z. Pan, Q. Shen, J. Sun, D. Long, H. Dong, L. Sun, X. Zhong, L.-J. Wan, J. Am. Chem. Soc. 138 (2016) 4201.
[12] Z. He, C. Zhong, S. Su, M. Xu, H. Wu, Y. Cao, Nat. Photon. 6 (2012) 591.
[13] Q. An, F. Zhang, J. Zhang, W. Tang, Z. Deng, B. Hu, Energy Environ. Sci. 9 (2016) 281.
[14] M.M. Lee, J. Teuscher, T. Miyasaka, T.N. Murakami, H.J. Snaith, Science 338 (2012) 643.
[15] H.-S. Kim, C.-R. Lee, J.-H. Im, K.-B. Lee, T. Moehl, A. Marchioro, S.-J. Moon, R. Humphry-Baker, J.-H. Yum, J.E. Moser, M. Grätzel, N.-G. Park, Sci. Rep. 2 (2012) 591.
[16] M. Park, H.J. Kim, I. Jeong, J. Lee, H. Lee, H.J. Son, D.-E. Kim, M.J. Ko, Adv. Energy. Mater. 5 (2015) 1501406.
[17] M. Park, J.-Y. Kim, H.J. Son, C.-H. Lee, S.S. Jang, M.J. Ko, Nano Energy 26 (2016) 208.
[18] P. Qin, S. Tanaka, S. Ito, N. Tetreault, K. Manabe, H. Nishino, M.K. Nazeeruddin, M. Grätzel, Nat. Commun. 5 (2014) 3834.
[19] J.-H. Im, I.-H. Jang, N. Pellet, M. Grätzel, N.-G. Park, Nat. Nanotech. 9 (2014) 927.
[20] D.P. McMeekin, G. Sadoughi, W. Rehman, G.E. Eperon, M. Saliba, M.T. Hörantner, A. Haghighirad, N. Sakai, L. Korte, B. Rech, M.B. Johnston, L.M. Herz, H.J. Snaith, Science 151 (2016) 151.
[21] A. Fujishima, Nature 238 (1972) 37.
[22] G. Wang, H. Wang, Y. Ling, Y. Tang, X. Yang, R.C. Fitzmorris, C. Wang, J.Z. Zhang, Y. Li, Nano Lett. 11 (2011) 3026.
[23] J. Zhang, Q. Xu, Z. Feng, M. Li, C. Li, Angew. Chem. Int. Ed. 120 (2008) 1766.
[24] K. Sivula, F. Formal, M. Grätzel, ChemSusChem 4 (2011) 432.
[25] H. Jun, B. Im, J.Y. Kin, Y.-O. Im, J.-W. Jang, E.S. Kim, J.Y. Kim, H.J. Kang, S.J. Hong, J.S. Lee, Energy Environ. Sci. 5 (2012) 6375.
[26] S.C. Warren, K. Voitchovsky, H. Dotan, C.M. Leroy, M. Cornuz, F. Stellacci, C. Hébert, A. Rothschild, M. Grätzel, Nat. Mater. 12 (2013) 842.
[27] K. Maeda, T. Takata, M. Hara, N. Saito, Y. Inoue, H. Kobayashi, K. Domen, J. Am. Chem. Soc. 127 (2005) 8286.
[28] Y. Qiu, K. Yan, H. Deng, S. Yang, Nano Lett. 12 (2012) 407.
[29] M. Seol, J.-W. Jang, S. Cho, J.S. Lee, K. Yong, Chem. Mater 25 (2013) 184.
[30] J. Su, L. Guo, N. Bao, C.A. Grimes, Nano Lett. 11 (2011) 1928.
[31] S.J. Hong, S. Lee, J.S. Jang, J.S. Lee, Energy Env. Sci. 4 (2011) 1781.
[32] M.D. Respinis, G.D. Temmerman, I. Tanyeli, M.C.M. Sanden, R.P. Doerner, M.J. Baldwin, R.V.D. Krol, ACS Appl. Mater. Interfaces 5 (2013) 7621.
[33] F.F. Abdi, R.V.D. Krol, J. Phys. Chem. C 116 (2012) 9398.
[34] F.F. Abdi, L. Han, A.H.M. Smets, M. Zeman, B. Dam, R.V.D. Krol, Nat. Commun. 4 (2013) 2195.
[35] R. Li, F. Zhang, D. Wang, J. Yang, M. Li, J. Zhu, X. Zhou, H. Han, C. Li, Nat. Commun. 4 (2013) 1432.
[36] M. Zhong, T. Hisatomi, Y. Kuang, J. Zhao, M. Liu, A. Iwase, Q. Jia, H. Nishiyama, T. Minegishi, M. Nakabayashi, N. Shibata, R. Niishiro, C. Katayama, H. Shibano, M. Katayama, A. Kudo, T. Yamada, K. Domen, J. Am. Chem. Soc. 137 (2015) 5053.
[37] Y. Kuang, Q. Jia, H. Nishiyama, T. Yamada, A. Kudo, K. Domen, Adv. Energy Mater. 6 (2016) 1501645.
[38] Q. Wang, T. Hisatomi, Q. Jia, H. Tokudome, M. Zhong, C. Wang, Z. Pan, T. Takata, M. Nakabayashi, N. Shibata, Y. Li, I.D. Sharp, A. Kudo, T. Yamada, K. Domen, Nat. Mater. 15 (2016) 611.
[39] X. Peng, L. Manna, W. Yang, J. Wickham, E. Scher, A. Kadavanich, A.P. Alivisatos, Nature 404 (2000) 59.
[40] J. Joo, H.B. Na, T. Yu, J. Yu, Y.W. Kim, F. Wu, J.Z. Zhang, T. Hyeon, J. Am. Chem. Soc. 125 (2003) 11100.
[41] O.E. Semonin, J.M. Luther, S. Choi, H.-Y. Chen, J. Gao, A.J. Nozik, M.C. Beard, Science 334 (2011) 1530.
[42] J.-W. Lee, D.-Y. Son, T.K. Ahn, H.-W. Shin, I.Y. Kim, S.-J. Hwang, M.J. Ko, S. Sul, H. Han, N.-G. Park, Sci. Rep. 3 (2013) 1050.
[43] J. Yang, J.-Y. Kim, J.H. Yu, T.-Y. Ahn, H. Lee, T.-S. Choi, Y.-W. Kim, J. Joo, M.J. Ko, T. Hyeon, Phys. Chem. Chem. Phys. 15 (2013) 20517.
[44] H. McDaniel, N. Fuke, N.S. Makarov, J.M. Pietryga, V.I. Klimov, Nat. Commun. 4 (2013) 2887.
[45] C. Cheng, S.K. Karuturi, L. Liu, J. Liu, H. Li, L.T. Su, A.Y. Tok, H.J. Fan, Small 8 (2012) 37.
[46] Y. Jin-nouchi, T. Hattori, Y. Sumida, M. Fujishima, H. Tada, ChemPhysChem 11 (2010) 3592.
[47] Y.-L. Lee, C.-F. Chi, S.-Y. Liau, Chem. Mater. 22 (2010) 922.
[48] D. Ding, Y. Chen, P. Lv, H. Yao, Y. Mu, S. Su, X. Zhang, L. Zhou, W. Fu, H. Yang, RSC Adv. 5 (2015) 6462.
[49] H.M. Chen, C.K. Chen, Y.-C. Chang, C.-W. Tsai, R.-S. Liu, S.-F. Hu, W.-S. Chang, K.-H. Chen, Angew. Chem. Int. Ed. 49 (2010) 5966.
[50] Y. Choi, M. Beak, K. Yong, Nanoscale 6 (2014) 8914.
[51] Z. Zhang, C. Gao, Z. Wu, W. Han, Y. Wang, W. Fu, X. Li, E. Xie, Nano Energy 19 (2016) 318.
[52] Z. Pan, I. Mora-Seró, Q. Shen, H. Zhang, Y. Li, K. Zhao, J. Wang, X. Zhong, J. Bisquert, J. Am. Chem. Soc. 136 (2014) 9203.
[53] P.K. Santra, P.V. Kamat, J. Am. Chem. Soc. 134 (2012) 2508.
[54] N. Zhou, G. Chen, X. Zhang, L. Cheng, Y. Luo, D. Li, Q. Meng, Electrochem. Commun. 20 (2012) 97.
[55] V. González-Pedro, C. Sima, G. Marzari, P.P. Boix, S. Giménez, Q. Shen, T. Dittrich, I. Mora-Seró, Phys. Chem. Chem. Phys. 15 (2013) 13835.
[56] A. Braga, S. Giménez, I. Concina, A. Vomiero, I. Mora-Seró, J. Phys. Chem. Lett. 2 (2011) 454.
[57] H.-J. Koo, J. Park, B. Yoo, K. Yoo, K. Kim, N.-G. Park, Inorg. Chim. Acta 361 (2008) 677.
[58] S. Ito, K. Nazeeruddin, P. Liska, P. Comte, R. Charvet, P. Péchy, M. Jirousek, A. Kay, S.M. Zakeeruddin, M. Grätzel, Prog. Photovoltaics: Res. Appl. 14 (2006) 589.
[59] S. Zhang, X. Yang, Y. Numata, L. Han, Energy Environ. Sci. 6 (2013) 1443.
[60] S. Ito, S.M. Zakeeruddin, R. Humphry-Baker, P. Liska, R. Charvet, P. Comte, M.K. Nazeeruddin, P. Pechy, M. Takata, H. Miura, S. Uchida, M. Grätzel, Adv. Mater. 18 (2006) 1202.
[61] A. Ghicov, S.P. Albu, R. Hahn, D. Kim, T. Stergiopoulos, J. Kunze, C.-A. Schiller, P. Falaras, P. Schmuki, J. Chem Asian 4 (2009) 520.
[62] Y. Diamant, S. Chappel, S.G. Chen, O. Melamed, A. Zaban, Coord. Chem. Rev. 248 (2004) 1271.
[63] B. Hyun, Y. Zhong, A.C. Bartnik, L. Sun, H.D. Abruna, F.W. Wise, J.D. Goodreau, J.R. Matthews, T.M. Leslie, N.F. Borrelli, ACS Nano 2 (2008) 2206.
[64] S. Luo, H. Shen, W. Hu, Z. Yao, J. Li, D. Oron, N. Wang, H. Lin, RSC Adv. 6 (2016) 21156.
[65] C.V.V.M. Gopi, M. Venkata-Haritha, S.-K. Kim, H.-J. Kim, Dalton Trans. 44 (2015) 630.
[66] T. Shen, J. Tian, L. Lv, C. Fei, Y. Wang, T. Pullerits, G. Cao, Electrochim. Acta 191 (2016) 62.
[67] J. Luo, H. Wei, Q. Huang, X. Hu, H. Zhao, R. Yu, D. Li, Y. Luo, Q. Meng, Chem. Commun. 49 (2013) 3881.
[68] R. Reiche, R. Thielsch, S. Oswald, K. Wetzig, J. Electron Spectrosc. Relat. Phenom. 104 (1999) 161.
[69] H. Qian, L. Li, J. Ren, Mater. Res. Bull. 40 (2005) 1726.
[70] D.S. Kim, Y.J. Cho, J. Park, J. Yoon, Y. Jo, M.-H. Jung, J. Phys. Chem. C 111 (2007) 10861.
[71] G. Yang, B. Yang, T. Xiao, Z. Yan, Appl. Surf. Sci. 283 (2013) 402.
[72] Y. Mikhlin, A. Kuklinskiy, E. Mikhlina, V. Kargin, I. Asanov, J. Appl. Electrochem. 34 (2004) 37.
[73] R. Holm, X-Ray Photoelectron Spectroscopy, Department of Applied Physics, Bayer AG, Leverkusen, Germany, 2016, pp. 37–72 Ch. 2.
[74] C. Pliangos, I.V. Yentekakis, S. Ladas, C.G. Vayenas, J. Catal. 159 (1996) 189.
[75] N. Ohtsu, N. Masahashi, Y. Mizukoshi, K. Wagatsuma, Langmuir 25 (2009) 11586.
[76] C. Viornery, Y. Chevolot, D. Léonard, B.-O. Aronsson, P. Péchy, H.J. Mathieu, P. Descouts, M. Grätzel, Langmuir 18 (2002) 2582.
[77] A. Nakahira, T. Kubo, C. Numako, ACS Appl. Mater. Interfaces 2 (2010) 2611.
[78] M. Kosmulski, Adv. Colloid Interface Sci. 99 (2002) 255.
[79] J.-W. Lee, J.-D. Hong, N.-G. Park, Chem. Commun. 49 (2013) 6448.
[80] J. Miao, H.B. Yang, S.Y. Khoo, B. Liu, Nanoscale 5 (2013) 11118.